

# Light-harvesting with guide-slide superabsorbing condensed-matter nanostructures

W. M. Brown<sup>1,\*</sup> and E. M. Gauger<sup>1,†</sup>

<sup>1</sup>*SUPA, Institute of Photonics and Quantum Sciences,  
Heriot-Watt University, Edinburgh, EH14 4AS, United Kingdom*

(Dated: May 16, 2022)

We establish design principles for light-harvesting antennae whose energy capture scales super-linearly with system size. Controlling the absorber dipole orientations produces sets of ‘guide-slide’ states which promote steady-state superabsorbing characteristics in noisy condensed-matter nanostructures. Inspired by natural photosynthetic complexes, we discuss the example of ring-like dipole arrangements and show that, in our setup, vibrational relaxation enhances rather than impedes performance. Remarkably, the superabsorption effect proves robust to  $\mathcal{O}(5\%)$  disorder simultaneously for all relevant system parameters, showing promise for experimental exploration across a broad range of platforms.

*Introduction* – Photosynthesis not only powers most life on Earth [1] but may also provide templates for artificial light-harvesting [2–4]. Recent years have seen many proposals for enhancing the performance of quantum photocells beyond the venerable Shockley-Queisser bound which limits traditional photovoltaic devices [5]. Many of these aim to prevent recombination once a photon has been absorbed, e.g. through interference in multi-level systems [6, 7] or as dark-state protection with multiple interacting dipoles [8–11]. Optical ratcheting [12, 13] may offer further advantages by allowing an antenna to keep absorbing whilst being immune to recombination. There is also evidence that coherent vibrations can be beneficial [14, 15].

An alternative approach to improving the performance of light harvesters would be to enhance optical absorption. In 1954 Dicke predicted the phenomenon of superradiance, where  $N$  atoms exhibit a collectively-enhanced ‘greater-than-the-sum-of-its-parts’ emission rate  $\propto N^2$  [16]. The possibility of harnessing the time-reversed phenomena has recently been proposed: (slightly) lifting degeneracies through symmetric dipolar interactions allows environmental control which temporarily keeps the system a regime where it displays ‘superabsorption’ [17]. This was inspired by photosynthetic ring antenna surrounding a reaction centre that converts optically-created excitations into useful chemical energy [18, 19]. In natural rings, dipoles tend to align tangentially around the ring [20], limiting the overall light-matter coupling but safeguarding against photo-damage [21]. We shall see that for artificial systems, other configurations with a stronger collective dipole prove more advantageous.

In this Letter, we examine the potential of condensed-matter nanostructures to operate as collectively-enhanced quantum photocells. Finding that the geometry proposed in Ref. [17], where all optical dipoles in the ring are aligned, fails in the presence of vibrational relaxation, we focus on a different means of achieving a *guide-slide superabsorption*. We define a guide-slide superabsorber to be a collection of optical dipoles with the

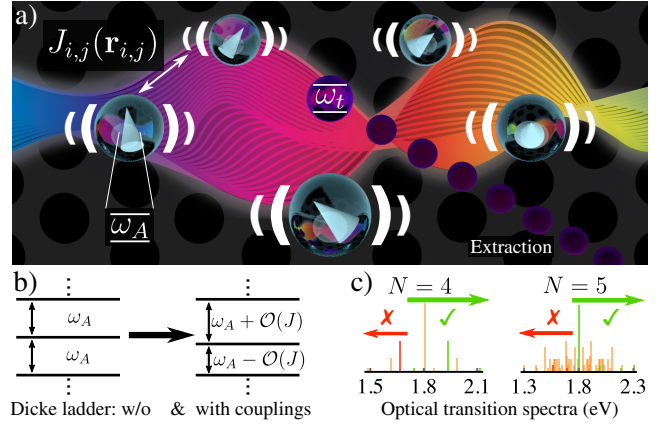


FIG. 1. a) Artistic depiction of a guide-slide superabsorber: A ring of skewed optical dipoles interacting with a collective thermalised photon environment, as well as local phonon baths and with a central extracting trap. A photonic crystal suppresses interaction with certain optical modes. b) Couplings  $J_{i,j}$  between dipoles cause a perturbation to the Dicke ladder, primarily lifting the degeneracy of ladder rung spacings. c) Histogram of transition frequencies for coupled dipoles, showing that there is no overlap between undesirable modes to be suppressed (red) and light-harvesting target modes (green).

following properties:

- I. A ladder of excitation manifolds, each with rapid relaxation to a well-defined lowest energy state.
- II. Collectively-enhanced optical rates link the lowest energy states of adjacent manifolds.
- III. Spectral selectivity allows suppression of optical decay below such an enhanced target transition.

We argue that the example of ring-like arrangements of dipoles can indeed meet the above conditions provided their dipoles are suitably oriented with skewed alignment. While the theoretical enhancement achievable with guide-slide superabsorption (GS-SA) trails behind that of the fully parallel case ( $\parallel$ -SA), crucially it

proves robust against the inclusion of phonons and significant levels of disorder: in the following we demonstrate superlinear scaling of both optical absorption and net power output in this configuration.

*Model* – We consider a ring of  $N$  optical dipole absorbers (see Fig. 1a), each modelled as a degenerate two-level system (2LS) with transition energy  $\omega_A = 1.8$  eV ( $\hbar = 1$ ), near the peak of the solar power spectrum. Letting  $N$  uncoupled dipoles interact collectively with the electromagnetic environment leads to a Dicke ladder with  $N + 1$  equally spaced ‘rungs’ separated by steps of  $\omega_A$ . Each rung represents a collective state for a different number of shared excitations, and optical rates near the middle of this ladder are collectively-enhanced and proportional to  $N^2$  [16, 22].

Interactions between dipoles perturb this picture, however, for moderate coupling strength, the ring system retains a ladder of eigenstates connected by collectively-enhanced optical transitions (Fig. 1b). The rungs are no longer evenly spaced, instead we obtain a chirped profile with a frequency increment determined by the strength of the dipolar couplings [17]. This is accompanied by a partial re-distribution of the oscillator strength away from ladder transitions, and a richer optical spectrum (Fig. 1c).

For closely spaced absorbers, dipolar interactions arise naturally as a result of ‘cross Lamb-shift’ (or resonant Förster) terms in the collective many-body quantum optical master equation [23–25],

$$J_{i,j}(\mathbf{r}_{i,j}) = \frac{1}{4\pi\epsilon_0|\mathbf{r}_{i,j}|^3} \left( \mathbf{d}_i \cdot \mathbf{d}_j - \frac{3(\mathbf{r}_{i,j} \cdot \mathbf{d}_i)(\mathbf{r}_{i,j} \cdot \mathbf{d}_j)}{|\mathbf{r}_{i,j}|^2} \right),$$

where  $\mathbf{r}_{i,j}$  is the vector linking the two dipoles  $i, j$ , and  $\mathbf{d}_i$  is the dipole moment at site  $i$  whose strength is related to the natural lifetime  $\tau_L$  of an isolated 2LS by  $|\mathbf{d}| = \sqrt{3\pi\epsilon_0\tau_L^{-1}c^3/\omega_A^3}$  [26, 27].

The ring Hamiltonian including pairwise interactions (and employing the usual definition of site-defined Pauli operators) reads ( $\hbar = 1$ )

$$\hat{H}_{\text{ring}} = \omega_A \sum_{i=1}^N \hat{\sigma}_i^z + \sum_{i,j=1}^N J_{i,j}(\mathbf{r}_{i,j}) (\hat{\sigma}_i^+ \hat{\sigma}_j^- + \hat{\sigma}_i^- \hat{\sigma}_j^+). \quad (1)$$

Assuming a ring diameter that is small compared to relevant photon wavelengths ( $\sim 2\pi c/\omega_A$ ) we can neglect phase factors in the coupling elements and write the optical interaction Hamiltonian as

$$\hat{H}_{I,\text{opt}} = \sum_{i=1}^N \mathbf{d}_i \hat{\sigma}_i^x \otimes \sum_k f_k (\hat{a}_k + \hat{a}_k^\dagger), \quad (2)$$

where  $f_k$  and  $\hat{a}_k^{(\dagger)}$  are, respectively, the coupling strength and annihilation (creation) operator for the optical mode  $k$  [17, 25].

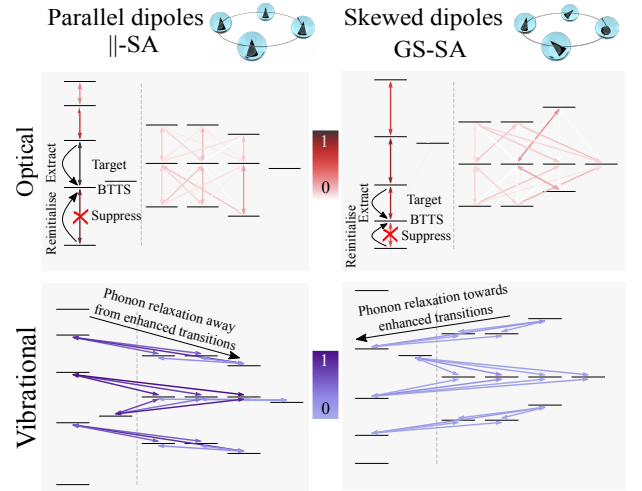


FIG. 2. Process diagram showing optical (red, top) and vibrational (blue, bottom) processes linking the eigenstates for a quadmer in the ||-SA (left) and GS-SA (right) setup. The states are organised in manifolds corresponding to the number of excitations in the system (with shown energetic spacings between manifolds not to scale compared to the manifold heights). Optical processes link different manifolds whereas vibrational ones act ‘sideways’. Superabsorption is achieved by pairing a reinitialisation process with a suppression of optical decay below the collectively-enhanced ‘target’ transition. The GS-SA system is stabilised by vibrational relaxation, whereas for ||-SA phonons are detrimental, pulling the system away from superabsorbing states.

We begin by contrasting the case of ||-SA, with all dipoles perpendicular to the plane of the ring, to GS-SA, where each dipole has been tilted ‘sideways’ by  $\theta_{\text{zen}} = \pi/4$  (see Fig. 1a and Supplementary Information (SI) [28]). The purpose of this tilting is to flip the sign of nearest-neighbour  $J_{i,j}$  terms in Eq. (1) whilst preserving a substantial collective dipole strength  $\mathbf{D} = \sum_i \mathbf{d}_i$ .

Transforming Eq. (2) into the eigenbasis of Eq. (1) reveals connections between ring eigenstates by optical processes. This is shown in the top panels of Fig. 2 for the case of an  $N = 4$  ring (quadmer) for both the ||-SA and the GS-SA configuration, in the latter case only for the ‘collective dipole’  $\mathbf{D}$  (but a full map is given in the SI [28]). States linked by collectively-enhanced transitions – which overlap significantly with Dicke ladder states (*cf.* Fig. 1b) – are shown in the left-most columns, and we shall henceforth refer to these as *ladder states*. The colour shading indicates the relative strengths of the transition matrix elements [29]. It is important to note that the ||-SA ladder states possess the highest energy in their respective excitation manifold, whereas the opposite is the case for GS-SA.

Reflecting the condensed-matter nature of typical nanostructures, we introduce local vibrational baths

which are generically coupled to each 2LS via [30]:

$$\hat{H}_{I,vib} = \sum_{i=1}^N \hat{\sigma}_i^z \otimes \sum_q g_{i,q} (\hat{b}_{i,q} + \hat{b}_{i,q}^\dagger), \quad (3)$$

where  $g_{i,q}$  and  $\hat{b}_{i,q}^{(\dagger)}$  are, respectively, the coupling strength and annihilation (creation) operator for the phonon mode  $q$  for the bath associated with site  $i$  [12, 25].

The bottom panels of Fig. 2 show the resulting phonon processes linking quadmer eigenstates for ||-SA and GS-SA, colour-coded to indicate relative strength [31]. Phonon processes only link states within the same excitation manifold and typically occur on a much faster timescale than optical processes. Obeying detailed balance, vibrational relaxation preferentially occurs ‘downwards’ in energy [32, 33]. For ||-SA this implies that phonons exert a pull away from the ladder linked by enhanced optical processes, effectively ruining the suitability of this configuration for steady-state superabsorbing behaviour (full details in the SI [28]). By contrast, for GS-SA, dissipative vibrational processes guide the system back to this ladder. A ring of skewed dipoles therefore meets all requirements I-III listed above, and from hereon we shall focus on such a GS-SA system.

We wish to benefit from the large oscillator strength in the middle of the ladder and thus define a ‘target transition’ with frequency  $\omega_{\text{good}}$ . As states near the middle of the ladder are not naturally substantially populated, additional measures are required for pinning the system at the ‘bottom-of-the-target-transition-state’ (BTTS). Following Ref. [17], spectral selectivity permits the application of environmental suppression of certain optical modes. Let the frequency of the ladder transition immediately below the BTTS be  $\omega_{\text{bad}}$ . Given a sufficient gap between  $\omega_{\text{good}}$  and  $\omega_{\text{bad}}$  (brought about by the strong enough  $|J_{i,j}|$  terms, see Fig. 1b), optical decay from the BTTS can be suppressed using a photonic band-gap environment. Fig. 1c shows that the transition frequencies of upwards absorption (green) and downwards emission (red) processes from the BTTS are indeed well-separated, meaning suppression of a single band of wavelengths will be effective: for GS-SA one may thus suppress all modes with frequency  $\omega < (\omega_{\text{good}} + \omega_{\text{bad}})/2$  (see Fig. 1c). A detailed discussion of the suppression of optical processes is given in the SI [28].

Suppressing emission from the BTTS prolongs the system’s proclivity for remaining in this state, keeping it primed for superabsorbing behaviour. However, an initially excited ring will nonetheless relax towards the ground state at long times. Addressing this issue requires controlled excitation pushing the ring system towards the centre of the ladder. This can be modelled, in an idealised fashion, as incoherent pumping with rate  $\gamma_r$  along the strongest collectively enhanced transitions from the ground state upwards to the BTTS. Alternatively, we also consider pumping the individual dipoles

in the SI [28]. We shall find that a suitable combination of suppression and reinitialisation achieves a steady-state solution with significant population in the BTTS.

To extract the energy of absorbed photons, we introduce a central trap that is equidistant from all absorbers, analogously to a photosynthetic reaction centre [18, 19]. Following the quantum heat engine model [7, 8, 34], the trap is modelled as a 2LS with energy  $\omega_t = \omega_{\text{good}}$ , whose (incoherent) decay to the ground state at rate  $\gamma_t$  represents the energy conversion process. For simplicity, we follow Refs. [8, 10, 11, 14] by implementing an incoherent transfer from the ring to the trap: a Lindblad process takes the ring from the top target transition state to the BTTS, while exciting the trap. In the SI we show that coherent ring-to-trap coupling results in the same qualitative behaviour [28].

Defining the steady-state population of the trap’s excited and ground states as  $\langle \rho_\alpha \rangle_{SS}$  and  $\langle \rho_\beta \rangle_{SS}$ , respectively, we assign a hypothetical current and voltage [7, 34]

$$I = e\gamma_t \langle \rho_\alpha \rangle_{SS}, \quad eV = \omega_t + k_B T_{\text{vib}} \ln \left( \frac{\langle \rho_\alpha \rangle_{SS}}{\langle \rho_\beta \rangle_{SS}} \right), \quad (4)$$

where  $k_B$  is Boltzmann’s constant and  $T_{\text{vib}} = 300$  K is the ambient (phonon) temperature. The second term in the voltage expression ensures thermodynamic consistency (see SI [28]). Optimising the ‘load’ via  $\gamma_t$  yields the maximally achievable output power  $P_{\text{max}} = I(\gamma_t^*) \cdot V(\gamma_t^*)$  at optimal  $\gamma_t^*$ . To obtain the net power of such a photocell, we must account for the energetic expenditure associated with the reinitialisation process. To this end, we apply a similar concept to the reinitialisation process: we assign a voltage and (upwards current) for each ladder step below the BTTS and sum over the respective products to obtain the total reinitialisation power [35].

We now proceed to solve the dynamics using a Bloch-Redfield approach [25]: non-secular Bloch-Redfield dissipators are formed from the optical, Eq. (2), and vibrational, Eq. (3), Hamiltonians. Apart from the (half-sided) photonic band-gap, we use the free-space optical spectral density, and assume radiative equilibrium with the sun,  $T = 5800$  K [12, 36]. Phonon processes are based on an Ohmic room-temperature bath, with typical rates exceeding optical ones by three orders of magnitude. Further dissipators describe extraction, trap decay and reinitialisation processes. The extraction rate  $\gamma_x$  is chosen comparable to that of typical phonon processes. The steady state of the system is then obtained as the nullspace of the total Liouvillian; full details of this process, all parameters, photon and phonon spectral densities, and the explicit master equation can be found in the SI [28].

*Results* – First we explore the interplay between the degree of suppression and reinitialisation power. Fig. 3a shows the net power produced by a pentamer as a function of degree of suppression and reinitialisation rate: for poor suppression, the system easily leaks down from the

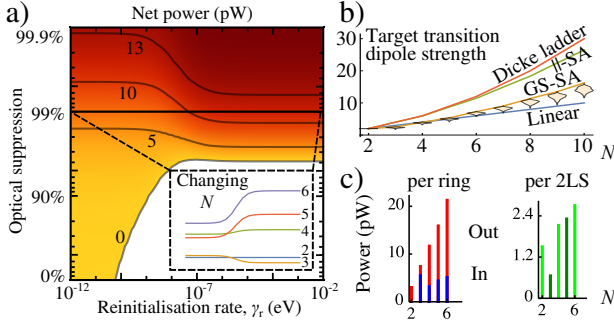


FIG. 3. a) Net power produced by a pentamer as a function of decay suppression and reinitialisation rate. The inset shows the 99% cross-section across the same reinitialisation range for different  $N$  (in arbitrary units). b) Scaling of oscillator strength of the light-harvesting target-transition with system size for different scenarios discussed in the main text. The GS-SA case includes distributions for 5% disorder introduced across model parameters (10 000 trials for up to  $N = 7$ , then 1 000, 500 and 50 trials for  $N = 8, 9, 10$ , respectively). c) Output and input power for different system sizes with 99% suppression of undesired optical modes, and superlinear growth of net power per site. Full details of the parameters used are in the SI [28].

BTTS, resulting in little (yellow) or even negative net power (white region) for slow and fast reinitialisation, respectively. By contrast, for high suppression the guide-slide effect successfully produces positive net power. In this regime, reinitialisation is worthwhile, so unsurprisingly faster reinitialisation improves performance further.

To demonstrate superabsorption, i.e. superlinear scaling of photon absorption and energy conversion, we now investigate the effect of increasing the ring-size  $N$ . Fig. 3b shows target transition oscillator strength as a function of  $N$ : we see that GS-SA displays superlinear scaling for  $N > 3$  but trails behind  $||$ -SA and the uncoupled Dicke model [37], due to a combination of employing interacting and skewed dipoles. In light of the fact that the Dicke model is unsuitable for absorption and  $||$ -SA breaks in the presence of vibrational relaxation, GS-SA remains the only contender offering superior scaling over the classical linear increase. Encouragingly, this GS-SA advantage persists upon introducing 5% normally-distributed disorder amongst relevant parameters (energy splittings  $\omega_A$ , natural lifetimes  $\tau_L$ , positions  $\mathbf{r}_i$ , and dipole orientations), as shown by the pale distribution marks. Further information regarding disorder can be found in the SI [28].

Focusing on the generated net power, the inset of Fig. 3a shows the transition into the guide-slide regime for  $2 \leq N \leq 7$  as a function of  $\gamma_r$  for fixed suppression at 99%. Once  $\gamma_r$  becomes large enough to compensate for (suppressed) optical leakage from the BTTS, larger rings do indeed achieve higher net power. This superlinear growth of the net power with  $N$  is confirmed by Fig. 3c,

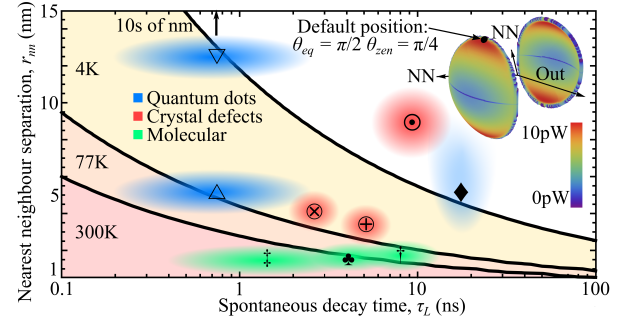


FIG. 4. Map of where a quadmer produces net power as a function of 2LS natural lifetime and nearest neighbour separation. Overlaid we also indicate regions typical of potential candidate systems: Adjacent ( $\nabla$ ) and stacked ( $\triangle$ ) self-assembled InGaS quantum dots [38, 39].  $\diamond$ : Colloidal quantum dots [40, 41].  $\odot$ : Nitrogen vacancies [42–44].  $\otimes$ : Silicon vacancy centres [45–47].  $\oplus$ : Phosphorous defects [48–50].  $\clubsuit$ : BODIPY dye [51–54].  $\dagger$ : Porphyrin rings [55–57].  $\ddagger$ : Mero-cyanine dye (H-aggregate) and pseudoisocyanine chloride (J-aggregate) [58–61]. Inset: dependence of net power produced on dipole offset angles. Arrows direct to nearest neighbours and to direction out of ring. Peak values in the red regions extend over a moderately broad angular range.

which also gives a breakdown of input vs output power. We note that the dimer and trimer are special: the former performs well as it does not require reinitialisation, whereas the latter has insufficient collective-enhancement for making active reinitialisation worthwhile (but performs adequately left to its own devices, see SI [28]). Beyond  $N > 3$ , however, there is an increasing trend of guide-slide superabsorption enabling quantum-enhanced photocell performance.

Taking a quadmer as the smallest working guide-slide superabsorber, we explore the temperature dependence of the effect. As a function of the 2LS spontaneous emission time  $\tau_L$  and nearest neighbour separation  $|\mathbf{r}_{i,i+1}|$  – the key parameters which determine the oscillator and Förster coupling strengths – we map out the region achieving net positive power for different phonon temperatures in Fig. 4. For this purpose, the dipole orientation angles were optimised, but never departed far from our previously employed (slightly sub-optimal) ad-hoc choice of  $\theta_{eq} = \pi/2, \theta_{zen} = \pi/4$ . For completeness, the inset of Fig. 4 shows a typical dependence of net power on the dipolar offset angles. Fig. 4 shows that cooling below room temperature expands the working range of GS-SA, since a colder phonon environment boosts the directionality of ‘guide-sliding’ onto ladder states even for closely spaced levels within the manifold (i.e. weaker Förster couplings).

To address the question of potential candidate systems suitable for exploring the GS-SA effect, we indicate regions and data-points referring to the properties of several state-of-the-art platforms for nanostructure photon-



ics. This demonstrates a broad range of credible building blocks for GS-SA antennae, leaving the key challenges of (i) ring assembly with control over the direction of the optical dipoles, (ii) embedding into a suitably engineered photonic environment, and (iii) furnishing the antennae with energy extraction and reinitialisation channels. Finally, of particular relevance to molecular systems, exciton-exciton annihilation needs to be controlled or avoided [12].

*Summary* – We have proposed a set of robust intuitive requirements for guide-slide superabsorption. We have shown that a combination of frequency-selective photonic band-gap suppression and reinitialisation results in a superabsorbing steady-state, characterised by a superlinear scaling of optical absorption and net power conversion with increasing system size. Inspired by photosynthetic structures, we have presented an example ring-system exhibiting this effect. Our proposed setup not only remains viable in the presence of phonons, but even benefits from vibrational relaxation. Further, the effect proves remarkably robust to substantial amounts of disorder and realistic imperfections, showing promise for experimental exploration across a number of platforms. Importantly, bio-inspired molecular rings, similar to the ones described in Refs. [55, 56], could function at room-temperature, offering an exciting perspective for quantum-enhanced light-harvesting and organic photovoltaics.

We thank Dale Scerri for useful discussions. W.M.B. acknowledges studentship funding from EPSRC under grant no. EP/L015110/1. E.M.G. thanks the Royal Society of Edinburgh and the Scottish Government for support.

---

\* Electronic address: wmb1@hw.ac.uk

† Electronic address: e.gauger@hw.ac.uk

- [1] R. E. Blankenship, *Molecular mechanisms of photosynthesis*, 2nd ed. (John Wiley & Sons, 2014).
- [2] G. D. Scholes, G. R. Fleming, A. Olaya-Castro, and R. van Grondelle, *Nat. Chem.* **3**, 763 (2011).
- [3] E. Romero, V. I. Novoderezhkin, and R. van Grondelle, *Nature* **543**, 355 EP (2017).
- [4] G. D. Scholes, G. R. Fleming, L. X. Chen, A. Aspuru-Guzik, A. Buchleitner, D. F. Coker, G. S. Engel, R. van Grondelle, A. Ishizaki, D. M. Jonas, J. S. Lundeen, J. K. McCusker, S. Mukamel, J. P. Ogilvie, A. Olaya-Castro, M. A. Ratner, F. C. Spano, K. B. Whaley, and X. Zhu, *Nature* **543**, 647 EP (2017).
- [5] W. Shockley and H. J. Queisser, *Journal of Applied Physics J. Appl. Phys. J. Appl. Phys. Appl. Phys. Lett.* **32** (1961), 10.1063/1.3583587.
- [6] M. O. Scully, *Phys. Rev. Lett.* **104**, 207701 (2010).
- [7] M. O. Scully, K. R. Chapin, K. E. Dorfman, M. B. Kim, and A. Svidzinsky, *Proceedings of the National Academy of Sciences of the United States of America* **108**, 15097 (2011).
- [8] C. Creatore, M. A. Parker, S. Emmott, and A. W. Chin, *Physical Review Letters* **111**, 253601 (2013).
- [9] Y. Yamada, Y. Yamaji, and M. Imada, *Physical Review Letters* **115**, 197701 (2015).
- [10] A. Fruchtmann, R. Gómez-Bombarelli, B. W. Lovett, and E. M. Gauger, *Physical Review Letters* **117**, 203603 (2016).
- [11] Y. Zhang, S. Oh, F. H. Alharbi, G. S. Engel, and S. Kais, *Phys. Chem. Chem. Phys.* **17**, 5743 (2015).
- [12] K. D. B. Higgins, B. W. Lovett, and E. M. Gauger, *The Journal of Physical Chemistry C* **121**, 20714 (2017).
- [13] Y. Zhang, A. Wirthwein, F. H. Alharbi, G. S. Engel, and S. Kais, *Phys. Chem. Chem. Phys.* **18**, 31845 (2016).
- [14] N. Killoran, S. F. Huelga, and M. B. Plenio, *The Journal of Chemical Physics* **143**, 155102 (2015), <http://dx.doi.org/10.1063/1.4932307>.
- [15] R. Stones, H. Hossein-Nejad, R. van Grondelle, and A. Olaya-Castro, *ArXiv e-prints* **arXiv:1601.05260** (2016), arXiv:1601.05260.
- [16] R. H. Dicke, *Physical Review* **93**, 99 (1954).
- [17] K. D. B. Higgins, S. C. Benjamin, T. M. Stace, G. J. Milburn, B. W. Lovett, and E. M. Gauger, *Nature Communications* **5**, 4705 (2014).
- [18] C. J. Law, A. W. Roszak, J. Southall, A. T. Gardiner, N. W. Isaacs, and R. J. Cogdell, *Molecular Membrane Biology* **21**, 183 (2004).
- [19] H. Sumi, *Chemical record* (New York, N.Y.) **1**, 480 (2001).
- [20] X. Hu, T. Ritz, A. Damjanović, and K. Schulten, *The Journal of Physical Chemistry B* **101**, 3854 (1997).
- [21] B. Kok, *Biochimica et Biophysica Acta* **21**, 234 (1956).
- [22] M. Gross and S. Haroche, *Physics Reports* **93**, 301 (1982).
- [23] G. V. Varada and G. S. Agarwal, *Physical Review A* **45**, 6721 (1992).
- [24] C. Curutchet and B. Mennucci, *Chemical Reviews* **117**, 294 (2017).
- [25] H.-P. Breuer and F. Petruccione, *The Theory of Open Quantum Systems* (Oxford University Press, 2002).
- [26] G. S. Agarwal (Springer, Berlin, Heidelberg, 1974) pp. 1–128.
- [27] V. N. Shatokhin, M. Walschaers, F. Schlawin, and A. Buchleitner, *ArXiv e-prints* **arXiv:1602.07878** (2016), arXiv:1602.07878.
- [28] See Supplemental Material at [URL will be inserted by publisher] for further detail, model extensions and disorder calculations.
- [29] These are symmetric with respect to absorption and emission (detailed balance follows from asymmetric rates), and they include the cubic frequency dependence of the free space spectral density of optical modes [25].
- [30] G. D. Mahan, *Many Particle Physics (Physics of Solids and Liquids)*, 3rd ed. (Springer, 2000).
- [31] This is based on an structureless Ohmic phonon spectral density.
- [32] E. M. Gauger and J. Wabnig, *Phys. Rev. B* **82**, 073301 (2010).
- [33] A. J. Ramsay, T. M. Godden, S. J. Boyle, E. M. Gauger, A. Nazir, B. W. Lovett, A. V. Gopal, A. M. Fox, and M. S. Skolnick, *Journal of Applied Physics* **109**, 102415 (2011), <https://doi.org/10.1063/1.3577963>.
- [34] K. E. Dorfman, D. V. Voronine, S. Mukamel, and M. O. Scully, *Proceedings of the National Academy of Sciences of the United States of America* **110**, 2746 (2013).
- [35] We have here dropped the second term in the voltage

- definition of Eq. (4). This is a conservative choice and errs on the side of caution: it will over- rather than underestimate the input power [28].
- [36] P. Würfel and U. Würfel, *Physics of Solar Cells: From Basic Principles to Advanced Concepts*, 3rd ed. (Wiley-VCH, 2016).
  - [37] Note that the gradient changes every two data points since the target transition lies at the centre of the ladder for a ring with an odd  $N$ , whereas for an even-sized ring it sits just below the middle.
  - [38] M. Creasey, J.-H. Lee, Z. Wang, G. J. Salamo, and X. Li, *Nano Letters* **12**, 5169 (2012).
  - [39] B. D. Gerardot, S. Strauf, M. J. A. de Dood, A. M. Bychkov, A. Badolato, K. Hennessy, E. L. Hu, D. Bouwmeester, and P. M. Petroff, *Physical Review Letters* **95**, 137403 (2005).
  - [40] B. Lounis, H. Bechtel, D. Gerion, P. Alivisatos, and W. Moerner, *Chemical Physics Letters* **329**, 399 (2000).
  - [41] S. B. Brichkin and V. F. Razumov, *Russian Chemical Reviews* **85**, 1297 (2016).
  - [42] A. Albrecht, G. Koplovitz, A. Retzker, F. Jelezko, S. Yochelis, D. Porath, Y. Nevo, O. Shoseyov, Y. Paltiel, and M. B. Plenio, *New Journal of Physics* **16**, 093002 (2014).
  - [43] P. Neumann, R. Kolesov, B. Naydenov, J. Beck, F. Rempp, M. Steiner, V. Jacques, G. Balasubramanian, M. L. Markham, D. J. Twitchen, S. Pezzagna, J. Meijer, J. Twamley, F. Jelezko, and J. Wrachtrup, *Nature Physics* **6**, 249 (2010).
  - [44] A. Angerer, K. Streltsov, T. Astner, S. Putz, H. Sumiya, S. Onoda, W. J. Munro, K. Nemoto, J. Schmiedmayer, and J. Majer, *ArXiv e-prints arXiv:1802.07100* (2018), arXiv:1802.07100.
  - [45] L. Rogers, K. Jahnke, T. Teraji, L. Marseglia, C. Müller, B. Naydenov, H. Schauffert, C. Kranz, J. Isoya, L. McGuinness, and F. Jelezko, *Nature Communications* **5**, 4739 (2014).
  - [46] A. Sipahigil, R. E. Evans, D. D. Sukachev, M. J. Burek, J. Borregaard, M. K. Bhaskar, C. T. Nguyen, J. L. Pacheco, H. A. Atikian, C. Meuwly, R. M. Camacho, F. Jelezko, E. Bielejec, H. Park, M. Lončar, and M. D. Lukin, *Science (New York, N.Y.)* **354**, 847 (2016).
  - [47] K. J. Morse, R. J. S. Abraham, A. DeAbreu, C. Bowness, T. S. Richards, H. Riemann, N. V. Abrosimov, P. Becker, H.-J. Pohl, M. L. W. Thewalt, and S. Simmons, *Science Advances* **3**, e1700930 (2017).
  - [48] J. L. O'Brien, S. R. Schofield, M. Y. Simmons, R. G. Clark, A. S. Dzurak, N. J. Curson, B. E. Kane, N. S. McAlpine, M. E. Hawley, and G. W. Brown, *Physical Review B* **64**, 161401 (2001).
  - [49] M. Fuechsle, J. A. Miwa, S. Mahapatra, H. Ryu, S. Lee, O. Warschkow, L. C. L. Hollenberg, G. Klimeck, and M. Y. Simmons, *Nature Nanotechnology* **7**, 242 (2012).
  - [50] S. R. Schofield, N. J. Curson, M. Y. Simmons, F. J. Rueß, T. Hallam, L. Oberbeck, and R. G. Clark, *Physical Review Letters* **91**, 136104 (2003).
  - [51] M. Y. Berezin and S. Achilefu, *Chemical reviews* **110**, 2641 (2010).
  - [52] I. Pochorovski, T. Knehans, D. Nettel, A. M. Müller, W. B. Schweizer, A. Caffisch, B. Schuler, and F. Diederich, *Journal of the American Chemical Society* **136**, 2441 (2014).
  - [53] S. Acikgoz, G. Aktas, M. N. Inci, H. Altin, and A. Sanyal, *The Journal of Physical Chemistry B* **114**, 10954 (2010).
  - [54] P.-H. Chung, C. Tregidgo, and K. Suhling, *Methods and Applications in Fluorescence* **4**, 045001 (2016).
  - [55] M. C. O'Sullivan, J. K. Sprafke, D. V. Kondratuk, C. Rinfray, T. D. W. Claridge, A. Saywell, M. O. Blunt, J. N. O'Shea, P. H. Beton, M. Malfois, and H. L. Anderson, *Nature* **469**, 72 (2011).
  - [56] J. K. Sprafke, D. V. Kondratuk, M. Wykes, A. L. Thompson, M. Hoffmann, R. Drevinskas, W.-H. Chen, C. K. Yong, J. Kärnbratt, J. E. Bullock, M. Malfois, M. R. Wasielewski, B. Albinsson, L. M. Herz, D. Zigmantas, D. Beljonne, and H. L. Anderson, *Journal of the American Chemical Society* **133**, 17262 (2011).
  - [57] J. Yu, X. Wang, B. Zhang, Y. Weng, and L. Zhang, *Langmuir* **20**, 1582 (2004).
  - [58] U. Rösch, S. Yao, R. Wortmann, and F. Würthner, *Angewandte Chemie International Edition* **45**, 7026 (2006).
  - [59] F. Würthner, *Accounts of Chemical Research* **49**, 868 (2016).
  - [60] Y. Obara, K. Saitoh, M. Oda, and T. Tani, *International journal of molecular sciences* **13**, 5851 (2012).
  - [61] H. von Berlepsch, C. Böttcher, and L. Dähne, *The Journal of Physical Chemistry B* **104**, 8792 (2000).

# Supplementary Information: Light-harvesting with guide-slide superabsorbing condensed-matter nanostructures

## INTRODUCTION

This supporting documentation contains full details of the model used in the main text, including tables listing a full set parameters for all figures. In particular, it includes more detail on the light-matter and inter-dipole coupling for non-parallel optical dipoles, the construction of the optical and vibrational Bloch-Redfield tensors, and our method for finding steady state solutions. Further, we explicitly demonstrate the breakdown of  $||$ -SA and the robustness of GS-SA in the presence of phonons, as well as confirming the integrity of superlinear GS-SA scaling for a range of extensions and variations of the model from the main text. Finally, we give a detailed discussion of the disorder applied to the GS-SA model, finding that it takes disorder of order 10% or more to break the principles enabling GS-SA introduced in the main text.

## OPTICAL CONTROL AND COUPLING

### GS-SA complete optical process map

The optical process map for GS-SA presented in Fig. 2 of the main text only accounts for the collective coupling (in the direction perpendicular to the plane of the ring of antennae),  $\mathbf{D} = \sum_i^N \mathbf{d}_i$ , which 71% of the overall dipole moment aligns with. The collective enhancement which we are primarily interested in can be sufficiently explained using just this shared direction, but our model also accounts for coupling in the plane of the ring. The overlap of optical dipole directions in the plane of the ring means that for GS-SA one no longer has the total optical separation of symmetric and non-symmetric states that is present in  $||$ -SA (denoted by the vertical dashed line in the figure). A complete process map of all optical processes is given in Fig. S1.

### Photonic band-gap suppression

To apply optical suppression for GS-SA, we define a cut-off frequency as the midpoint between the transition frequency for the target transition,  $\omega_{\text{good}}$ , and the frequency associated with the transition below the bottom of target transition state (BTTS) down to the rung beneath,  $\omega_{\text{bad}}$ . Any optical process with an associated transition frequency which is smaller than the cut-off will be suppressed. Naturally, this suppression affects both the up and down rates of the processes.

This cut-off frequency definition implies that all the collectively enhanced optical transitions will be suppressed beneath the target transition, as well as relaxation to any other (off-ladder) state in the manifold below. This relies on the fact that in GS-SA, the non-degenerate, enhanced optical transition frequencies increase as one moves up the ladder, as can be seen by the spacings of the states in Fig. 2 of the main text. For the case of  $||$ -SA, a similar process can be applied if instead one suppresses all modes *above* a certain threshold rather than below.

In reality, photonic band-gaps are of finite width (and often not of perfect square well form) as opposed to a binary partition of frequency space. A wide enough band-gap may nevertheless suppress all ladder transitions below the BTTS. However, whether or not that is the case, we find our approach works well as long as emission at frequency  $\omega_{\text{bad}}$  and its immediate vicinity is adequately suppressed.

### “Free” ratcheting reinitialisation

Analysing the complete optical process map in Fig. S1, we see that for GS-SA there are additional optical pathways. In the main text we focussed only on the collectively-enhanced optical transitions, linking states which are optically disconnected from ‘off-ladder’ system eigenstates. For GS-SA, however, each (bottom of excitation manifold) ladder state is optically connected to the other states in adjacent manifolds above as well as below.

As mentioned above, beneath the target transition in

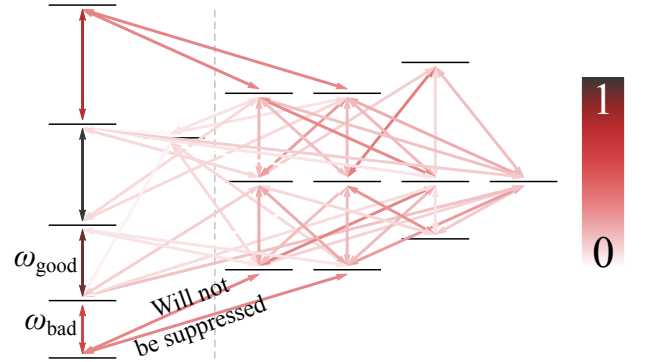


FIG. S1. The optical process map for a GS-SA quadmer with the same parameters as those used in Fig. 2 of the main text. All processes arising from the coupling Hamiltonian (and included in our numerical model) are shown. Notably, several processes now cross the dashed dividing line. The colouring of each line denotes the relative strength of each process, normalised against the strongest process on the map. For clarity, energy separations between the different states in this image are not to scale: intra-band spacings have been scaled up with respect to interband spacings.

GS-SA the suppression covers all transitions from the ladder states to the entirety of the manifold below, and is thus effective for all possible decay pathways. By contrast, processes linking ladder states to higher energy off-ladder states in the manifold above are not necessarily suppressed: these transitions can potentially have a frequency larger than the cut-off, meaning optical excitation to the manifold above remains possible. If such an excitation occurs, then rapid phonon relaxation takes the system down to the bottom of the new manifold, from where optical relaxation is suppressed, but excitation is once more still possible. This mechanism allows for the system to climb the ladder without external reinitialisation. The quality of this self ladder climbing depends on the strength of the suppression.

In the main text, Fig. 3a shows this effect: for negligibly small reinitialisation the net power produced increases as suppression strength increases. The inset of Fig. 3a, showing net power as a function of reinitialisation rate, also demonstrates this effect, demonstrating that as the external reinitialisation process begins to dominate over naturally occurring ‘free’ reinitialisation for  $\gamma_r \gtrsim 10^{-6}$  eV. Further, comparing different  $N$  at 99% suppression, we observe that free reinitialisation works well for climbing up to two manifolds. Finally, one can see that for the trimer, the cost of having fast external reinitialisation to steer more of the system into the superabsorbing regime is not worth the gains in power produced, since the net power actually decreases in this regime. This is understandable by a combination of the free reinitialisation only having to bridge one rung, and the limited collective enhancement of a small trimer system.

This mechanism of free reinitialisation is reminiscent of the optical ratcheting effect proposed by Ref. [S1], however with an inverted energy landscape in each excitation manifold due to the change of sign of dipole-dipole couplings (in molecular language effectively corresponding to a switch from H- to J-aggregate character). A further difference is that the present effect requires a photonic band-gap in the current setup, as opposed to Ref. [S1].

## OPTICAL AND VIBRATIONAL DISSIPATORS

Our approach for dealing with the optical and vibrational environments closely follows the methods outlined in Ref. [S2].

## Electromagnetic environment

As a starting point for dealing with the optical environment, we take our optical interaction Hamiltonian,

$$\hat{H}_{I,opt} = \sum_{i=1}^N \mathbf{d}_i \hat{\sigma}_i^x \otimes \sum_k f_k (\hat{a}_k + \hat{a}_k^\dagger), \quad (S1)$$

and rewrite the individual dipoles’  $\hat{\sigma}^x$  operators in terms of system eigenbasis states [using the matrix diagonalising the Hamiltonian Eq. (1) of the main text]. This yields the optical transitions between the system eigenstates. Reflecting the vectorial nature of the optical dipoles, each term is a 3-vector, with one element per Cartesian direction of the optical field. It is easy to see that optical transitions will only link eigenstates from different (adjacent) excitation manifolds and cannot give rise to intra-manifold transitions.

The system operators (in the eigenbasis) of the light matter interaction can be written as a Hermitian matrix with each element being a 3-vector. Terms beneath the diagonal represent processes which lower the system energy whereas those above raise it. By taking a list of all processes, i.e. all non-zero vectors in this matrix, we form the (non-secular) Bloch-Redfield tensor (in the Schrödinger picture):

$$\begin{aligned} \mathcal{D}_{opt} = \sum_{n,m} \mathbf{d}_n \cdot \mathbf{d}_m & \left( A_m(\omega_m) \rho_S(t) A_n^\dagger(\omega_n) \Gamma_{nm}(\omega_m) \right. \\ & + A_n(\omega_n) \rho_S(t) A_m^\dagger(\omega_m) \Gamma_{nm}^\dagger(\omega_m) \\ & - \rho_S(t) A_m^\dagger(\omega_m) A_n(\omega_n) \Gamma_{nm}^\dagger(\omega_m) \\ & \left. - A_n^\dagger(\omega_n) A_m(\omega_m) \rho_S(t) \Gamma_{nm}(\omega_m) \right). \quad (S2) \end{aligned}$$

This includes all pairwise combinations of lowering (raising) processes  $A_\alpha^\dagger$  with associated frequency  $_{(-+)}\omega_\alpha$ . Every term in the above expression is weighted by the dot product of the two 3-vectors associated with the processes being paired. Note that here the  $\mathbf{d}_{n,m}$  no longer represent the dipole moments of individual dipoles but those associated with system energy eigenstates.

The above dissipator includes environmental correlation functions, evaluation of which yields the process rates. The correlation functions are

$$\begin{aligned} \Gamma_{nm}(\omega) &= \int_0^\infty ds e^{i\omega s} \langle B_n^\dagger(t) B_m(t-s) \rangle, \\ \Gamma_{nm}^\dagger(\omega) &= \int_0^\infty ds e^{-i\omega s} \langle B_m^\dagger(t-s) B_n(t) \rangle, \quad (S3) \end{aligned}$$

where the  $B(t)$  are the environment operators of the interaction Hamiltonian. Since all dipoles are assumed to be co-located at the same position (for the present purpose of deriving dissipative processes [S3] – we do allow for separation when calculating dipole-dipole interactions), there are no phase factors in coupling elements



and we can write a single joint correlation function of the general form [S4]

$$\Gamma_{n_im_j}(\omega) = \delta_{ij} \left( \frac{1}{2} \gamma(\omega) + iS(\omega) \right), \quad (\text{S4})$$

where

$$\gamma_{\text{opt}}(\omega) = \kappa_{\text{opt}} \omega^3 (1 + n(\omega)). \quad (\text{S5})$$

Here,  $\kappa_{\text{opt}}$  is determined by the lifetime  $\tau_L$  of an isolated 2LS with splitting  $\omega_A$ , such that  $\gamma_{\text{opt}}(\omega_A) = \tau_L^{-1}$  at zero temperature [so that  $n(\omega) = 0$ ]. The cubic frequency dependence of  $\gamma_{\text{opt}}(\omega)$  arises from the density of optical modes in free space, and the Bose-Einstein occupancy of photon modes  $n(\omega)$  is

$$n(\omega) = \frac{1}{e^{\beta \hbar \omega} - 1} \quad (\text{S6})$$

with  $\beta = 1/k_B T$ , where  $T$  is the photon bath temperature and  $k_B$  is Boltzmann's constant.

For the purpose of light harvesting, we set  $T = 5800$  K matching the solar temperature. This choice corresponds to being in radiative equilibrium with a black-body emitter at the temperature of the sun; the Supplement of Ref. [S1] contains a more detailed discussion of the implications of this assumption.

The correlation function's imaginary contribution  $S(\omega)$  results in unitary corrections to the Hamiltonian dynamics through generalised Lamb and Stark shift terms. The most important consequence of those is the cross Lamb-shift dipole-dipole interaction [S5], which we have already included explicitly in our ring Hamiltonian Eq. (1). By contrast, diagonal Lamb shift terms only slightly renormalise the transition energy itself and can be absorbed in the effect splitting of the dipoles. For these reasons, we here neglect  $S(\omega)$ .

Finally, all rates with an associated frequency below the suppression threshold have the photonic band-gap suppression applied, by multiplication with the respective suppression factor.

### Vibrational

The steps for finding the vibrational dissipator are similar to those taken for the optical one. We start with the spin-boson interaction Hamiltonian repeated across the  $N$  sites (labelled with index  $i$ ):

$$\hat{H}_{I,vib} = \sum_{i=1}^N \hat{\sigma}_i^z \otimes \sum_q g_{i,q} (\hat{b}_{i,q} + \hat{b}_{i,q}^\dagger). \quad (\text{S7})$$

An important difference to the optical case is that we now assume an independent phonon bath for each absorber. Hence, there will be no collective effects caused

by phonons. Rather, we treat each phonon bath separately (all being equivalent and thus identical copies of each other).

We now have a system interaction matrix for each system, which upon transformation to the system eigenbasis result in  $N$  matrices of raising and lowering processes between system eigenstates. For each matrix,  $\alpha$ , a list of all the processes is taken to form another non-secular Bloch-Redfield dissipative term:

$$\begin{aligned} \mathcal{D}_{\alpha,vib} = \sum_{n,m} w_n w_m & \left( A_m(\omega_m) \rho_S(t) A_n^\dagger(\omega_n) \Gamma_{nm}(\omega_m) \right. \\ & + A_n(\omega_n) \rho_S(t) A_m^\dagger(\omega_m) \Gamma_{nm}^\dagger(\omega_m) \\ & - \rho_S(t) A_m^\dagger(\omega_m) A_n(\omega_n) \Gamma_{nm}^\dagger(\omega_m) \\ & \left. - A_n^\dagger(\omega_n) A_m(\omega_m) \rho_S(t) \Gamma_{nm}(\omega_m) \right), \quad (\text{S8}) \end{aligned}$$

where the  $n, m$  summation covers all pairwise combinations of processes for that matrix, and the factors  $w_i$  reflect appropriate weightings arising from the transformation to the ring eigenbasis. The full vibrational dissipator is then given by the sum over  $\alpha$ ,

$$\mathcal{D}_{vib} = \sum_{\alpha}^N \mathcal{D}_{\alpha,vib}. \quad (\text{S9})$$

Since the environments for each set of terms can be considered identically, there is only form of correlation function to calculate:

$$\Gamma_{n_im_j}(\omega) = \delta_{ij} \left( \frac{1}{2} \gamma(\omega) + iS(\omega) \right). \quad (\text{S10})$$

Assuming a structureless Ohmic spectral density (see Sec. for other choices), we write

$$\gamma_{vib}(\omega) = \kappa_{vib} \omega (1 + n(\omega)), \quad (\text{S11})$$

where for now we let  $\kappa_{vib}$  be a phenomenologically motivated prefactor which sets the timescale of phonon rates. Reflecting the fact the vibrational processes typically occur on a much faster timescale than optical ones, we define  $\kappa_{vib} = 10^3 \times \gamma_{\text{opt}}(\omega_A) / \bar{\omega}_{vib}$ , where  $\bar{\omega}_{vib}$  represents the mean intra-excitation-manifold transition frequency. This ensures that (spontaneous) phonon emission at the average phonon energy proceeds with a rate that is 1000 times faster than the spontaneous photon emission time of an individual optical dipole.

The Bose-Einstein factor  $n(\omega)$  is defined as in the optical case but now for the temperature of the phonon bath at 300 K (except for Fig. 4 in the main text which explores different temperatures). As is the case with the optical dissipator, the imaginary component of the environment correlation functions is discarded.

## CALCULATING THE POWER OUTPUT

### Discussion of quantum heat engine approach

The quantum heat engine approach [S6, S7] is based on the idea of introducing an abstract two-level system ‘load’ (hereafter referred to as the ‘trap’) to a photocell as a means of obtaining a relationship between current and voltage. The ‘resistance’ of the load is tuneable by changing the phenomenological decay rate  $\gamma_t$  from the higher energy state  $|\alpha\rangle$  into the lower state  $|\beta\rangle$ . Scanning  $\gamma_t$  (typically through many orders of magnitude), one obtains an  $IV$ -curve, and via  $P = IV$  also the power as a function of voltage.

Specifically, the current is given by

$$I = e\gamma_t \langle \rho_\alpha \rangle_{SS} , \quad (\text{S12})$$

where  $\langle \rho_i \rangle_{SS}$  denotes the steady state population of the state  $i$ , and the effective potential difference is

$$eV = \hbar\omega_{\alpha\beta} + k_B T_{\text{vib}} \ln \left( \frac{\langle \rho_\alpha \rangle_{SS}}{\langle \rho_\beta \rangle_{SS}} \right) , \quad (\text{S13})$$

where  $\hbar\omega_{\alpha\beta}$  is the energy of the trap,  $k_B$  is Boltzmann’s constant, and  $T_{\text{vib}}$  is the ambient (phonon bath) temperature. The logarithmic term in the potential difference equation provides a correction to the effective voltage which is based on the deviation of the trap populations from the thermal distribution [S8]. Its inclusion ensures thermodynamic consistency: typically, the effective voltage  $V$  will be lower than  $\hbar\omega_{\alpha\beta}/e$ . This implicitly partitions the trap decay process into a heat and a work current contribution. By contrast, neglecting this partitioning may result in the thermodynamic inconsistencies described by Ref. [S9].

We employ this model for obtaining the generated power (‘Power out’) of our photocell devices. All results shown are obtained for a numerically optimised  $\gamma_t^*$  that delivers peak power at  $\max(I(\gamma_t^*) \cdot V(\gamma_t^*))$ .

For reinitialisation (‘Power in’), we distinguish two cases: (i) ‘ladder-climbing’ reinitialisation and (ii) site-based reinitialisation. For the latter case – employed in Secs. and of this document – we simply employ the same process in reverse, but this time separately for *each dipole*. Here, the roles of ‘upper’ and ‘lower’ level are swapped in Eqs. (S12) and (S13) to the dipoles’ ground and excited states, respectively. Additionally,  $\gamma_t$  in Eq. (S12) is replaced by the applied reinitialisation rate  $\gamma_r$ . The total input power is then given by the sum over the power terms associated with each dipole  $P_{\text{in}} = \sum_{i=1}^N I_i \cdot V_i = NI_0 V_0$  (the second equality follows in the absence of disorder when all dipoles are equivalent). Note that this particular type of reinitialisation indiscriminately moves the system up the next higher exciton manifolds, with no preference for populating ladder states. This is not a problem for GS-SA, where phonon

processes will let it slide back onto the ladder, but precludes its use for ||-SA.

For ladder-climbing reinitialisation – considered in the main paper – we instead calculate  $P_{\text{in}} = \sum_{n=1}^{\lfloor (N-1)/2 \rfloor} I_n \cdot V_n$ , where  $I_n$  is the upwards current of ladder rung  $n$  and  $V_n$  the associated voltage. Reinitialisation only takes place between the ground state and the BTTS (situated at rung  $\lfloor (N-1)/2 \rfloor$  counted from the bottom of the ladder). In this case the logarithmic term in Eq. (S13) is questionable, so we directly identify the respective ladder rung transition frequency as  $V_n$ . However, we have checked that inclusion of the logarithmic term over the range of applied  $\gamma_r$  only makes a negligible difference to the results (and leads to a marginally reduced input power). This not only confirms that our choice is conservative but further suggests that a thermodynamic correction is not required for our purpose.

### Quantum heat engine processes

Implementing the above-described quantum heat engine approach requires additional dissipators to be added to the master equation describing the dynamics of the ring antenna (as well as an extended Hilbert space dimension to accommodate the additional trap two level system).

These could be introduced through operationally motivated Lindblad dissipators of the generic form [S2]

$$\mathcal{D}_L[\rho, \gamma, \hat{L}] \equiv \gamma \left( \hat{L} \rho \hat{L}^\dagger - \frac{1}{2} \{ \hat{L}^\dagger \hat{L}, \rho \} \right) , \quad (\text{S14})$$

where  $\{\bullet, \star\} = \bullet\star + \star\bullet$  denotes the anti-commutator,  $\hat{L}$  is a Lindblad operator and  $\gamma$  its associated rate. However, in keeping with treating the optical and vibrational environment to Bloch-Redfield level of theory, we shall employ that approach for these dissipative terms as well, noting that in certain cases our approach automatically reduces to the simpler Lindblad form.

To construct the dissipator of incoherent processes, we start with a normalised interaction Hamiltonian (matrix)  $M$ , which features non-zero matrix transition elements connecting the desired levels. Upon transformation of this matrix into the system’s eigenbasis, we obtain the corresponding Bloch-Redfield dissipator by summing over all pairwise combinations of the non-zero interaction elements, yielding:

$$\begin{aligned} \mathcal{D}_{BR} = \gamma \sum_{n,m} \Theta(\sigma\omega_m) & \left( A_m(\omega_m) \rho_S(t) A_n^\dagger(\omega_n) \right. \\ & + A_n(\omega_n) \rho_S(t) A_m^\dagger(\omega_m) - \rho_S(t) A_m^\dagger(\omega_m) A_n(\omega_n) \\ & \left. - A_n^\dagger(\omega_n) A_m(\omega_m) \rho_S(t) \right). \end{aligned} \quad (\text{S15})$$

Here,  $\gamma$  is the phenomenological rate of the process and  $\Theta(\omega)$  is the Heaviside function (0 for  $\omega < 0$  and 1 for

$\omega \geq 0$ ). For  $\sigma = 1$  this ensures that only ‘downwards’ (decay) processes survive, whereas for  $\sigma = -1$  it is unidirectional in the ‘upwards’ direction (as will be required for reinitialisation pumping). It should be noted that since all these processes are one-way, we only take pairwise combinations of terms which both either raise or lower the system energy, creating a partial secular approximation.

#### Trap decay operator

As discussed above, the quantum heat engine ‘trap’ is a two-level system which undergoes incoherent decay from its excited state  $|\alpha\rangle$  to its ground state  $|\beta\rangle$ . This is accomplished by feeding the interaction matrix  $M = \hat{\sigma}_t^- + \hat{\sigma}_t^+$  [with  $\hat{\sigma}_t^- \equiv |\beta\rangle\langle\alpha|$  and  $\hat{\sigma}_t^+ = (\hat{\sigma}_t^-)^\dagger$ ] into Eq. (S15). Further, we set  $\sigma = 1$  (so that only the decay terms are effective) and choose  $\gamma_t$  as the decay rate.

For the case of incoherent extraction (see below), the above procedure results in the effective Lindblad dissipator  $\mathcal{D}_t := \mathcal{D}_L[\rho_S, \gamma_t, \hat{\sigma}_t^-]$ , whilst it retains a more general form for coherent extraction, when trap and ring eigenstates become intertwined.

Going beyond the canonical heat engine picture and with reference to the extraction chain depicted in Fig. 1 of the main text, we note that in the right limit, incoherent decay of a single 2LS can also qualitatively captures the effect of exciton transfer down a chain of sites in a tight-binding model [S10, S11].

#### Extraction operator

The extraction process transfers the excitation from the ring onto the trap. In the following we describe two ways of accomplishing this.

**Incoherent:** here we consider targeted extraction, which lowers the ring population from the eigenstate at the ‘top-of-the-target-transition’ (TTTS) to the BTTS, while at the same time exciting the trap from its ground state to its excited state. As we let the energy of the trap  $\omega_t$  match the transition frequency of the target transition  $\omega_{\text{good}}$  this process is energy conserving. Since this process is defined directly on eigenstates of ring and trap, there is no need to consider Eq. (S15) and we can directly write the Lindbladian dissipator  $\mathcal{D}_x = \mathcal{D}_L[\rho_S, \hat{L}_{\text{ex}}, \gamma_x]$  with  $\hat{L}_{\text{ex}} = |\text{BTTS}\rangle\langle\text{TTTS}| \otimes \hat{\sigma}_t^+$ .

This type of extraction underlies all results of main text and also the majority GS-SA (and ||-SA) results in this document, unless explicitly stated otherwise.

**Coherent:** Following the Supplement of Ref. [S5] we also investigate the effect of coherent Hamiltonian coupling between the ring and the trap, as an alternative model. This does not alter our core conclusions but requires a number adjustments of the model, so a full dis-

cussion of coherent extraction is given in its own section later in this document.

#### Reinitialisation operators

**Ladder-climbing:** for this reinitialisation method, we apply pumping to the BTTS from all lower energy ladder rungs. The corresponding Lindblad operators have the form  $\hat{M}_{n,\text{reinit}} = |\text{BTTS}\rangle\langle n|$  with  $n \in \{1, \lfloor (N-1)/2 \rfloor\}$  indicating the rung from which to climb. In the absence of coherent extraction, the resulting dissipator is  $\mathcal{D}_r = \sum_n \mathcal{D}_L[\rho_S, \hat{M}_{n,\text{reinit}}, \gamma_r]$ . In the presence of coherent extraction, a dissipator based on Eq. (S15) is formed for each  $n$  separately with interaction matrices  $\hat{M}_{n,\text{reinit}} + \hat{M}_{n,\text{reinit}}^\dagger$ , rate  $\gamma_r$ , and  $\sigma = -1$ . The sum over these is then the combined reinitialisation dissipator  $\mathcal{D}_r$ .

**Site-based:** for site-based reinitialisation we have  $N$  interaction matrices,  $M_{\alpha,\text{reinit}} = \hat{\sigma}_i^+ + \hat{\sigma}_i^-$ , where  $i \in \{1 \dots N\}$  indexes the ring sites. Each interaction matrix results in a dissipator term via Eq. (S15) with  $\sigma = -1$  and at rate  $\gamma_r$ . The sum over all these constitutes the total  $\mathcal{D}_r$ .

### FINDING THE STEADY STATE WITH THE LIOUVILLIAN

The overall master equation governing the dynamics of our ring antenna plus trap is ( $\hbar = 1$ )

$$\frac{d}{dt}\rho_S = -i[\hat{H}_S, \rho_S] + \mathcal{D}_{\text{opt}} + \mathcal{D}_{\text{vib}} + \mathcal{D}_x + \mathcal{D}_r + \mathcal{D}_t \quad (\text{S16})$$

and can be recast into the Liouvillian form

$$\frac{d}{dt}\rho_S = \mathcal{L}\rho_S \quad (\text{S17})$$

with the formal solution

$$\rho_S(t) = e^{\mathcal{L}t}\rho_S(0). \quad (\text{S18})$$

Diagonalising the Liouvillian, the master equation reads

$$\rho_S(t) = \begin{pmatrix} e^{\lambda_1 t} & 0 & \dots \\ 0 & e^{\lambda_2 t} & \dots \\ \vdots & \vdots & \ddots \end{pmatrix} \rho_S(0), \quad (\text{S19})$$

where  $\lambda_i$  are the complex eigenvalues of  $\mathcal{L}$ . Since in most cases all the eigenstates of our system are connected, there is a unique steady state, and thus only one zero-valued eigenvalue exists (all others having negative real parts). For  $t \rightarrow \infty$  only the eigenstate with associated  $\Re(\lambda) = 0$  survives. The steady state of the system is then given by this eigenvector, regardless of the initial system state.

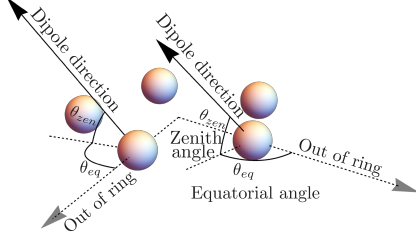


FIG. S2. Representation of the equatorial angle,  $\theta_{eq}$  and the zenith angle  $\theta_{zen}$ , used to define dipole directions.

For  $\parallel$ -SA without phonons and disorder (covered in Sec. ), the system eigenstates are not fully connected leading to multiple zero eigenvalues of the Liouvillian. In this case, obtaining the steady state is slightly more complicated and depends on the choice of initial state, which is the overall ground state in our case.

### FULL SET OF MODEL PARAMETERS

A complete set of model parameters used for the figures of the main text and this documents are printed in Tab. 1 and Tab. 2, respectively. Not shown is the trap decay rate  $\gamma_t$  as this is always numerically scanned over to find the value maximising the output power. For disorder calculations, the parameters are given by Gaussian distributions of varying widths (as stated in the relevant figures) around the indicated means.

In Fig. S2 we include a visual representation of the two angles used to define the dipole orientations. The equatorial angle,  $\theta_{eq}$ , gives rotation in the plane of the ring, and the zenith angle,  $\theta_{zen}$  gives inclination. The angles define a local reference for each dipole and chosen directions are constant rotations with respect to the ‘out-of-ring’ direction, as shown.

### BREAKDOWN OF PARALLEL SUPERABSORPTION ( $\parallel$ -SA)

In the main text we introduce two different ring setups,  $\parallel$ -SA and GS-SA.  $\parallel$ -SA implements the geometry proposed in Ref. [S5]. Having all dipoles parallel maximises the total collective dipole of the system, so this would seem like the obvious choice for boosting the absorption of the system. However, as briefly mentioned in the main text, the inclusion of rapid phonon relaxation spoils the effect entirely. In the following, we show this breakdown explicitly.

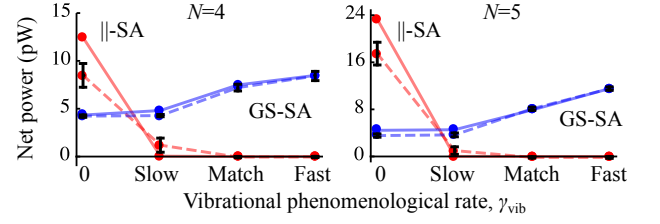


FIG. S3. Plots showing the net power produced by a quadmer and pentamer in  $\parallel$ -SA and GS-SA setups for different phonon rates. Fixed parameters are plotted with the bold lines, while the dashed lines use 1% input disorder over 100 trials (standard deviation error bars included).  $\parallel$ -SA produces larger powers only for negligibly small phonon coupling. By contrast, the GS-SA setup always produces positive net power, and only increases in performance when phonons dominate over photon processes.

Fig. SS3 shows the net power produced by a quadmer and a pentamer for four different phonon rates:

1.  $\kappa_{vib} = 0$ , i.e. no phonons;
2.  $\kappa_{vib} = 10^{-3} \times \gamma_{opt}(\omega_A)/\overline{\omega_{vib}}$  – ‘slow’;
3.  $\kappa_{vib} = \gamma_{opt}(\omega_A)/\overline{\omega_{vib}}$  – ‘match’;
4.  $\kappa_{vib} = 10^3 \times \gamma_{opt}(\omega_A)/\overline{\omega_{vib}}$  – ‘fast’.

Results for both  $\parallel$ -SA and GS-SA are shown with red and blue lines, respectively. Solid lines use fixed input parameters, while the dashed lines are averages from 100 trials with 1% disorder introduced over all input parameters (cf. Sec. ).

The  $\parallel$ -SA case produces large net power when there is either no phonon environment at all or if phonon rates are low compared to those of optical processes. In the presence of phonons, regardless of the phonon coupling strength,  $\parallel$ -SA requires some level of disorder, otherwise population gets trapped in off-ladder states from where it cannot decay. By not arriving back on the ladder it also will not be ‘picked up’ again by the ladder-climbing reinitialisation process. The steady-state of idealised  $\parallel$ -SA in the presence of any level of phonon coupling is therefore entirely on off-ladder states and away from enhanced optical transitions. For this reason the solid red line drops to zero as soon as phonons are included, whereas the dashed line (including a mild level of disorder) dips significantly but only hits zero once vibrational processes match optical ones. Both red lines tend towards zero for faster vibrational rates, demonstrating the breakdown of  $\parallel$ -SA. Overall, the above discussion suggests that  $\parallel$ -SA may be achievable for systems where no naturally prevalent phonon environment exists and / or where exquisite (reinitialisation) control is available, e.g. on the superconducting circuit QED platform [S12, S13].

Meanwhile for GS-SA the power produced increases in the presence of a dominant phonon environment, both



Variable	Symbol	Fig. 3a	Fig. 3a Inset	Fig. 3b	Fig. 3c	Fig. 4	Fig. 4 Inset
System size	$N$	5	Varied	Varied	Varied	4	4
2LS splitting	$\omega_A$	1.8 eV	1.8 eV	1.8 eV	1.8 eV	1.8 eV	1.8 eV
2LS lifetime	$\tau_L$	2.5 ns	2.5 ns	2.5 ns	2.5 ns	Varied	2.5 ns
2LS separation	$r_{nn}$	1 nm	1 nm	1 nm	1 nm	Varied	1 nm
Equatorial angle	$\theta_{eq}$	$\pi/2$	$\pi/2$	$\pi/2$	$\pi/2$	$\pi/2$	Varied
Zenith angle	$\theta_{zen}$	$\pi/4$	$\pi/4$	$\pi/4$	$\pi/4$	Optimised	Varied
Optical suppression	$S$	Varied	99%	n/a	99%	99%	99%
Extraction rate	$\gamma_x$	$10^{-2}$ eV	$10^{-2}$ eV	n/a	$10^{-2}$ eV	$10^{-2}$ eV	$10^{-2}$ eV
Reinitialisation rate	$\gamma_r$	Varied	Varied	n/a	$10^{-2}$ eV	$10^{-2}$ eV	$10^{-2}$ eV
Optical temperature	$T_{opt}$	5800 K	5800 K	5800 K	5800 K	5800 K	5800 K
Vibrational temperature	$T_{vib}$	300 K	300 K	300 K	300 K	300,77,4 K	300 K

TABLE I. Full set of model parameters for main text figures. Additionally, photon and phonon spectral densities as discussed in Sec. were employed.

Variable	Symbol	Fig. S2 GS	Fig. S2	Fig. S8, S9 & S10
System size	$N$	4,5	4,5	5
2LS splitting	$\omega_A$	1.8 eV*	1.8 eV*	1.8 eV*
2LS lifetime	$\tau_L$	2.5 ns*	2.5 ns*	2.5 ns*
2LS separation	$r_{nn}$	1 nm*	1 nm*	1 nm*
Equatorial angle	$\theta_{eq}$	$\pi/2^*$	$\pi/2^*$	$\pi/2^*$
Zenith angle	$\theta_{zen}$	$\pi/4^*$	$\pi/2^*$	$\pi/4^*$
Optical suppression	$S$	99%	99.9%	n/a
Extraction rate	$\gamma_x$	$10^{-2}$ eV	$10^{-2}$ eV	n/a
Reinitialisation rate	$\gamma_r$	$10^{-2}$ eV	$10^{-2}$ eV	n/a
Optical temperature	$T_{opt}$	5800 K	5800 K	n/a
Vibrational temperature	$T_{vib}$	300 K	300 K	n/a

TABLE II. Parameters for figures in this SI document. Figs. S4-S7 used the same parameters as Fig. 3c of the main text, other than the deviations mentioned in their respective captions. Asterisks denote values around which Gaussian distributions of varying width were taken in disorder trials.

in idealised and disordered cases. GS-SA also still performs adequately even in the absence of phonons or for low phonon rates, so unlike ||-SA it is not limited to a particular operating regime. However, as discussed in the main text, the tradeoff is that the maximum power produced from GS-SA cannot match that of ||-SA due to its reduced collective optical dipole. GS-SA's robustness to (and even benefitting from) vibrational relaxation suggests it may be suitable for implementation across a wide range of condensed-matter nanostructures, including in the solid state and for molecular systems.

## VARIANTS AND EXTENSIONS OF THE GS MODEL

### Different phonon spectral densities

In the main text, we chose an Ohmic phonon spectral density that was otherwise structureless, and in particular did not feature a high-frequency cut-off. Since the form of the phonon spectral density varies from system to system, we shall here present results when substituting this with a superohmic spectral density including a cut-off. Our results underline the robustness of the GS-SA approach and demonstrate that the results presented

in the main text are generic and did not derive from the particular choice of phonon environment.

We now consider phonon rates dependent on a spectral density in the usual way

$$\gamma(\omega) = J(\omega)(1 + N(\omega)) , \quad (S20)$$

where  $J(\omega)$  is the spectral density. Different functions could be used for the spectral density, with different forms being appropriate for different absorbing antennae. As long as the chosen phonon spectral density allows for relaxation processes to move population to the bottom of rungs, then the guide-slide concept still works. As an example we take the spectral density form

$$J(\omega) = \frac{\lambda\omega^3}{2\omega_{crit}^3} e^{-\frac{\omega}{\omega_{crit}}} , \quad (S21)$$

where  $\lambda$  denotes the reorganisation energy, and  $\omega_{crit}$  is the cut-off frequency. The bar charts in Fig. S4 show that the guide-slide states still display superabsorbing behaviour for two different choices of  $\lambda$  and  $\omega_{crit}$  that are appropriate for molecular systems [S14]. The right panel plots the spectral densities and a histogram of the different phonon transition frequencies in the quadmer and pentamer systems. The guide-slide effect requires overlap of the spectral density with (at least a sufficient subset of) vibrational frequencies to allow phonon-assisted

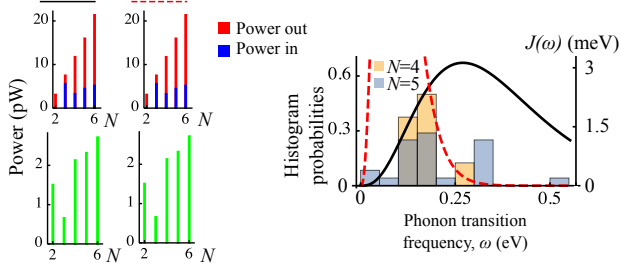


FIG. S4. **Left:** power in, out, and net power per site found for various systems sizes using the spectral density of Eq. (S21). The parameters used in the spectral density were  $\lambda = 5$  meV and  $\omega_{\text{crit}} = 90$  meV (left column, black line) and  $\lambda = 20$  meV and  $\omega_{\text{crit}} = 25$  meV (right column, red dashed line). **Right:** spectral densities overlaid on normalised histograms of the different phonon transition frequencies arising with the quadmer (yellow) and pentamer (blue). The other parameters are those of the inset of Fig. 3c in the main text.

relaxation onto the ladder states. Clearly, this is the case here and results in net power output scaling superlinearly with ring size as shown in left panel of Fig. S4.

#### Site-based reinitialisation

As a variation to the more idealised ladder-climbing reinitialisation, we also consider constant pumping across all of the absorbing sites on the ring. In this case, too rapid a reinitialisation rate leads to the system occupying the top half of the ladder, causing a waste of (input) power. In contrast to ladder-climbing reinitialisation, where we use a constant and sufficiently fast reinitialisation rate for all system sizes, we now trial different pumping rates, settling for the choice providing optimal net power performance.

Fig. S5 qualitatively reproduces the features of Fig. 3c in the main text, and in particular retains the superlinear scaling of net power output. The inset in Fig. S5 shows the drop off in net power when the system reinitialisation rate becomes too fast (leading to population inversion of the individual sites and substantial steady-state population above the ladder mid-point).

#### Coherent extraction process

As previously mentioned, coherent coupling between the ring and the trap increases the complexity of the calculations. However, once the right parameter regime has been identified, this does not drastically change the results.

To implement coherent extraction, the extraction dissipator,  $\mathcal{D}_x$ , is removed from Eq. (S16), and instead terms for moving population between the ring sites and the trap are added to the Hamiltonian:  $\sum_i^N \mathcal{C}_x (\hat{\sigma}_i^+ \hat{\sigma}_t^- + \hat{\sigma}_i^- \hat{\sigma}_t^+)$ ,

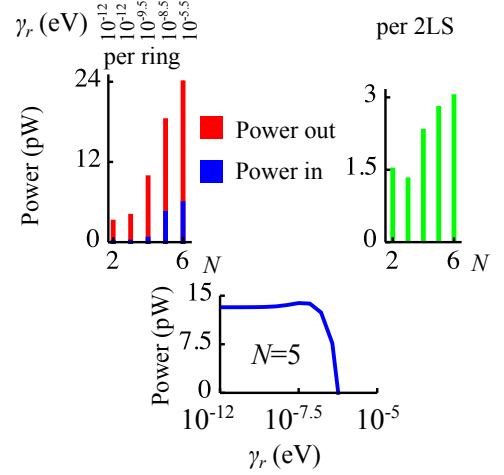


FIG. S5. Power input, output, and net power per site for site-based reinitialisation. In each case the reinitialisation rate which provides the optimal net power is used, the reinitialisation rate,  $\gamma_r$ , is shown across the top. Superlinear behaviour is unaffected by this change. Other parameters are those of the inset of Fig. 4 of the main text, except for an increased optical suppression of 99.9%. The inset shows how increasing the reinitialisation rate leads to an improvement in the power out for the pentamer before pushing the system in to the top half of the ladder and wasting energy.

where  $\mathcal{C}_x$  is the coupling strength between the ring and the trap. The trap site is kept degenerate with the target transition of the unperturbed ring eigenbasis (i.e. the in the absence of the trap),  $\omega_t = \omega_{\text{good}}$ .

Resonant coherent coupling between the target ring transition and the trap implies that we no longer have unidirectional extraction and population can return from the trap back to the ring. However, for adequately fast trap decay rate  $\gamma_t$ , this is suppressed and does not significantly affect the results.

For relatively small  $\mathcal{C}_x$  compared to  $J_{i,i+1}$ , the presence of the trap in the Hamiltonian can be understood as a minor perturbation of the ring eigenstates, and the trap will only resonantly extract energy from the target transition (as adjacent ladder transitions are sufficiently far detuned). However, as the coupling strength is increased, the trap and ring energy levels become hybridised. In this case the ‘trap’ begins to also extract from other ‘ladder transitions’. An important ramification of losing full extraction selectivity is that the trap starts pulling the the system down the ladder, undermining the photonic bandgap suppression and counteracting the reinitialisation process.

Nonetheless, in Fig. S6 we find that superabsorbing behaviour remains possible under coherent extraction. Here, the extraction coupling strength of  $10^{-4}$  eV is fast enough to extract most excitons absorbed by the system (for an optical bath at the solar surface temperature), while not being so strong as to break the selectivity of

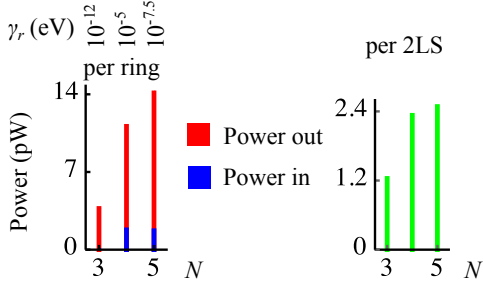


FIG. S6. Power input, output, and net power per site for coherent extraction between the trap and the ring. A slow extraction rate of  $10^{-4}$  eV is used to keep the extraction frequency selective (see text for discussion). Super-linear behaviour similar to that seen in Fig. 3c of the main text is observed in this case. For this plot different choices of  $\gamma_r$  were trialled, with selected rates as shown in the figure. The other parameters in these data runs are those used in Fig. 3c of the main text, except for the optical suppression which is here increased to 99.9%.

extraction from the target transition. This graph stops with the pentamer due to the substantial computational demand of solving the master equation for the case of a hexamer. The power values are not quite as high as those observed when incoherent coupling is used, as is to be expected due to the extraction speed restriction which we applied.

Note that this plot also does not include the case of a dimer: here, letting both dipoles pointing tangentially and inclined  $45^\circ$  out of the plane of the ring leads to vanishing dipole-dipole coupling between the absorbers as the dipoles are then strictly orthogonal. This entails that for even arbitrarily weak extraction coupling the degenerate trap and dimer states are maximally hybridised and the picture of viewing the trap as a perturbation to the ring antenna fails.

#### Coherent extraction & site-based reinitialisation

As a final variant of the model, we combine coherent extraction with site-based reinitialisation. In this setup, one needs to simultaneously ensure that the extraction coupling is not so strong that the trap starts extracting energy from other than the target transition, and that the reinitialisation proceeds fast enough to keep the system operating in the centre of the ladder, but not so fast as to push it further up.

The results of these data runs are shown in Fig. S7, and once more they display superabsorbing behaviour.

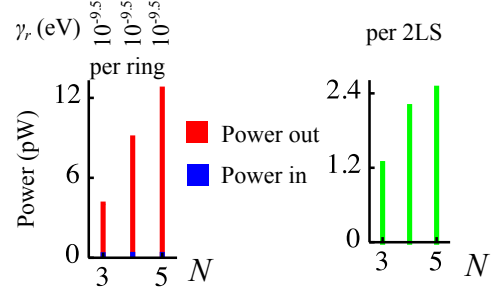


FIG. S7. Power input, output, and net power per site for coherent extraction and site-based reinitialisation. In each case the reinitialisation rate  $\gamma_r$  was optimised to maximise net generated power. Notably, the small optimal values of  $\gamma_r$  mean that the input power is also rather small. The other parameters in these data runs are consistent with those used in Fig. 3c of the main text, but again with optical suppression increased to 99.9%.

### GUIDE-SLIDE SUPERABSORPTION IN PRESENCE OF DISORDER

Finally we investigate the robustness of the GS-SA model when disorder is introduced. We look at how randomising the 2LS parameters affects the guide-slide effect by applying a normal distribution to relevant input variables: the 2LS energy splitting  $\omega_A$ , optical natural lifetime  $\tau_L = \gamma_{\text{opt}}(\omega_A)^{-1}$ , the  $x, y, z$  components of the dipole positions  $\mathbf{r}_i$ , and the dipole orientation of each 2LS via  $\theta_{\text{eq}}$  and  $\theta_{\text{zen}}$ . In an individual trial, all of these parameters are drawn from a normal distribution centred around the means given in Tab. II.

We have performed two types of disorder calculations: (i) simulations based on the full dynamic model and calculating the net power output of a disordered GS-SA (and ||-SA) photocell; the results are shown in Fig. S3 (ii) analysing disorder in our candidate ring antennae with skewed dipoles with respect to the three criteria enabling GS-SA introduced in the main text. The former results have already been discussed, so in the following we focus on the second approach.

To address property I from the main text, Fig. S8 shows the level structure of the skewed ring antennae under the influence of different amounts of disorder. The lowest energy in each excitation manifold, i.e. the ladder rungs, are represented by black lines, whilst all other levels in the same excitation manifold are displayed in red (for clarity offset to the right). The overall ground and fully excited states are manifolds with only a single level and thus have no associated ‘red boxes’. As before, the spacing between manifolds is not to scale.

The left panel shows how disorder causes a spreading of the black lines and red boxes. Keeping the ground state energy fixed, this spread amplifies in higher excited states. A key requirement for GS-SA is that the system will always be rapidly directed to the lowest energy

(ladder) state in each excitation manifold, requiring a sufficiently steep energy gradient (with steps larger than thermal energy to prevent phonon absorption). Encouragingly, there remains a clear vertical separation between black and red subset for 1% disorder, but seemingly the lines begin to overlap for 5% disorder, which appears to undermine property I. However, overlaying the entire ensemble is misleading in this regard: in the right panel of Fig. S8 we pin together the ladder states for each excitation manifold [S15]. This shows that the separation between black lines and red boxes survives for larger amounts of disorder. The black dashed line is elevated by 25 meV above the BTTS, so gives an indication of how likely thermal excitation away from the ladder state is at room temperature. Only a small subset of the 10% disorder trials are prone to having the desired ‘guide-sliding’ interfered with by thermal excitation, and in these cases a colder ambient temperature would resolve this problem. We conclude that our candidate for GS-SA continues to meet criterion I even in the presence of substantial amounts of disorder.

Fig. 3b of the main text includes disorder calculations regarding the strength of the optical transitions covering the target transition in GS-SA. This involves summing the transition strengths of the transitions from BTTS to any state in the rung above the BTTS (by the guide-slide mechanism any off-ladder population will swiftly phonon-relax back onto the ladder and be available for extraction from the TTTS). Fig. 3b considers the total useful transition strengths for different system sizes. For  $N = 2, \dots, 7$ , we averaged over 10 000 trials, while the average over 1 000, 500, and 50 trials underlies the octamer, nonamer, and decamer, respectively. For that figure of the main text, all systems parameters are drawn from a normal distribution with 5% standard deviation.

In Fig. S9 we focus on case of a pentamer and extend the 5% disorder datapoint from Fig. 3b to 1% and 10% disorder. Based on 1 000 trials, the different coloured histograms show the total transition strengths normalised against the maximum transition strength which would be expected of a pentamer in the interactionless Dicke model. We see that it takes disorder across all 2LS parameters in excess of 5% to fully spoil the advantage of collective-enhancement. We have a further requirement to bear in mind: the most enhanced transition should indeed be the one linking the BTTS and TTTS: for 1%, 5% and 10% disorder, this is the case for, respectively, 100%, 99.7% and 76.8% of trials. Note that for small amounts of disorder a tiny fraction of trials exceeds the ‘Fixed GS-SA’ line: this is since the tilting angles of the dipoles are set at a fixed value and have not been optimised, so that introducing some randomness can occasionally beat the not disordered benchmark. Fig. S9 thus demonstrates that our candidate superabsorber also displays robustness to substantial amounts of disorder with respect to criterion II.

Property III for GS-SA, spectral selectivity, is required to suppress coupling to certain optical modes, while allowing access to those needed to the collectively enhanced target transition. To achieve this there needs to be sufficient separation between the desired target transition frequency,  $\omega_{\text{good}}$ , and the largest undesirable frequency that needs to be suppressed,  $\omega_{\text{bad}}$ . Fig. S10 shows the difference between these values for differing amounts of disorder. Whilst the distribution of this gap widens with increasing amounts of disorder, reassuringly, there is no overlap and typical differences are in excess of several 10’s of meV, which provides the desired spectral selectivity and meets criterion III.

In summary, this section has analysed the effect of up to 10% disorder for a pentamer ring antennae with skewed dipoles, finding that criteria I and III continue being met for up to 10% and criterion II is robust to at least 5% disorder across the most relevant 2LS parameters simultaneously. Referring back to Fig. S3, we have observed that meeting the three criteria indeed translates into photocells with quantum-enhanced power generation performance. This confirms the potential of engineering and observing the GS-SA effect in real condensed-matter nanostructures.

---

\* Electronic address: wmb1@hw.ac.uk

† Electronic address: e.gauger@hw.ac.uk

- [S1] K. D. B. Higgins, B. W. Lovett, and E. M. Gauger, *The Journal of Physical Chemistry C* **121**, 20714 (2017).
- [S2] H.-P. Breuer and F. Petruccione, *The Theory of Open Quantum Systems* (Oxford University Press, 2002).
- [S3] This a good approximation as long as the separations between dipoles are much smaller than the wavelength of relevant photons.
- [S4] It should be noted that the  $\delta_{ij}$  in the correlation function is responsible for the dot product of the dipoles in the optical dissipator: it ensures that there is no contribution for pairs of terms pointing along orthogonal Cartesian directions.
- [S5] K. D. B. Higgins, S. C. Benjamin, T. M. Stace, G. J. Milburn, B. W. Lovett, and E. M. Gauger, *Nature Communications* **5**, 4705 (2014).
- [S6] M. O. Scully, *Phys. Rev. Lett.* **104**, 207701 (2010).
- [S7] K. E. Dorfman, D. V. Voronine, S. Mukamel, and M. O. Scully, *Proceedings of the National Academy of Sciences of the United States of America* **110**, 2746 (2013).
- [S8] C. Creatore, M. A. Parker, S. Emmott, and A. W. Chin, *Physical Review Letters* **111**, 253601 (2013).
- [S9] D. Gelbwaser-Klimovsky and A. Aspuru-Guzik, *Chem. Sci.* **8**, 1008 (2017).
- [S10] G. G. Giusteri, F. Mattiotti, and G. L. Celardo, *Phys. Rev. B* **91**, 094301 (2015).
- [S11] G. Schaller, G. G. Giusteri, and G. L. Celardo, *Phys. Rev. E* **94**, 032135 (2016).
- [S12] J. A. Mlynek, A. A. Abdumalikov, C. Eichler, and A. Wallraff, *Nature Communications* **5**, 5186 (2014).
- [S13] A. Potočník, A. Bargerbos, F. A. Y. N. Schröder, S. A.



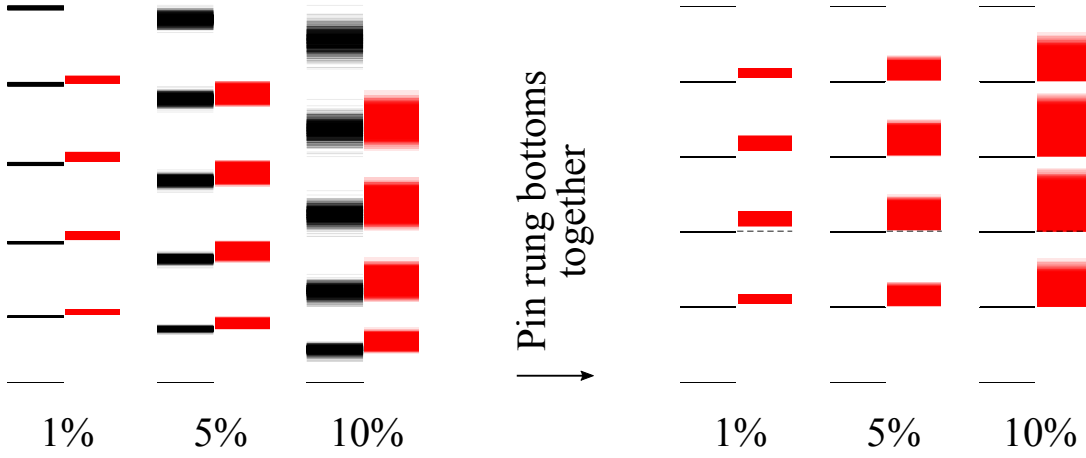


FIG. S8. Level structure of a pentamer with 1%, 5% and 10% input disorder averaged over 1000 trials. The top and bottom excitation manifolds are represented by single black lines, while the other manifolds feature single black lines for their lowest energy states, and a red box covering the energy range of the remaining states in the manifold. The spacing between manifolds is not to scale with the inter-manifold spacing. On the left, one sees the increased effect of disorder in higher up manifolds (due to the zero energy rung being the same position in all of the trials). To counteract this, on the right we pin together the black lines in each manifold, making the surviving separation between these and the red boxes more apparent. The dashed black line demonstrates the energetic step which could be overcome by room temperature thermal excitation.

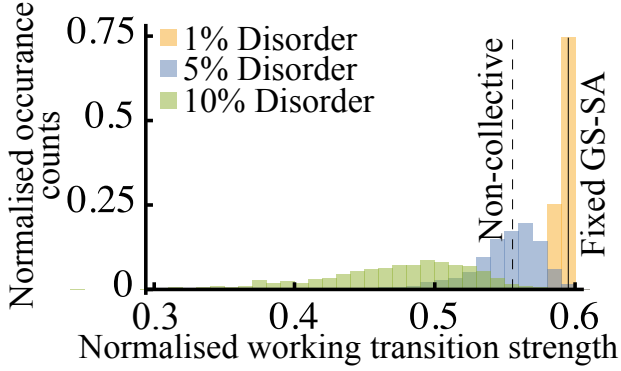


FIG. S9. Histograms of the maximal absorption transition strength for a pentamer with 1%, 5% and 10% input disorder over 1000 trials. The transition strengths are normalised against the (unachievable) transition strength found in the unperturbed Dicke model. Also indicated is the no disorder GS-SA case (solid black line), and the value expected for independent absorbers which do not collectively absorb (dashed line). It is important to note from Fig. 3b in the main text that the gap between the solid line and dashed line increases with increasing  $N$ .

- Khan, M. C. Collodo, S. Gasparinetti, Y. Salathé, C. Creatore, C. Eichler, H. E. Türeci, A. W. Chin, and A. Wallraff, *Nature Communications* **9**, 904 (2018).
- [S14] J. K. Sowa, J. A. Mol, G. A. D. Briggs, and E. M. Gauger, *Phys. Chem. Chem. Phys.* **19**, 29534 (2017).
- [S15] Pinning the ladder states shows the criterion can be met individually for each member of the ensemble. Meeting it simultaneously across a disordered ensemble may be more difficult, but as shown in the next section  $\omega_{\text{good}}$  and  $\omega_{\text{bad}}$  remain separated so that targeted suppression and extraction remain feasible.

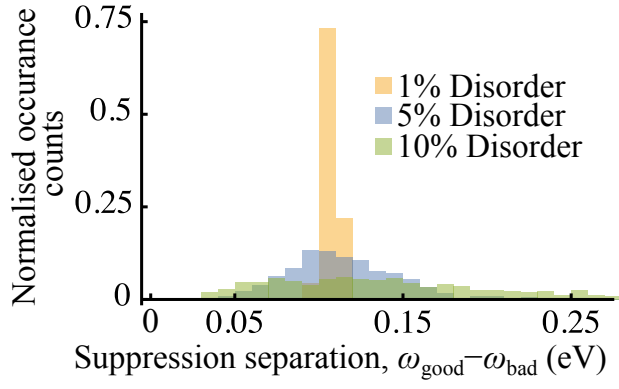


FIG. S10. Histograms of the frequencies used to define the optical cutoff frequency,  $\omega_{\text{good}}$  and  $\omega_{\text{bad}}$ , for a pentamer with 1%, 5% and 10% input disorder over 1000 trials. The optical cutoff frequency in GS-SA is defined as  $\frac{\omega_{\text{good}} + \omega_{\text{bad}}}{2}$ , so adequate separation is needed between these two frequencies.